Correction of anisoplanatic phase errors in digital holography

Samuel T. Thurman* and James R. Fienup

The Institute of Optics, University of Rochester, Rochester, New York 14627, USA
**Corresponding author: thurman@optics.rochester.edu*

Received October 29, 2007; accepted January 31, 2008;
posted February 20, 2008 (Doc. ID 89109); published March 27, 2008

The quality of coherent images computed from digital holography or heterodyne array data is sensitive to phase errors of the reference and/or object beams. A number of algorithms exist for correcting phase errors in or very near the hologram plane. In the case of phase errors introduced a nonnegligible distance away from hologram plane, the resulting imagery exhibits anisoplanatism. A feature of coherent imaging is that such phase errors may be corrected by simply propagating the aberrated fields (from the object) from the hologram plane to the plane where the phase errors were introduced and applying the phase-error correction algorithms to the fields in that plane. We present experimental results that demonstrate correction of such anisoplanatic phase errors. © 2008 Optical Society of America

OCIS codes: 090.1000, 090.1760, 100.3010, 100.3020, 100.3190.

Figure 1 shows an example of a recording geometry for a digital hologram of an object. A beam splitter divides a collimated beam of monochromatic light, reflecting part of the beam to a reference flat and transmitting the remainder of the beam so as to illuminate a diffuse object. Light reflected off of the reference flat is reflected by a second beam splitter to a detector array. Light reflected/scattered by the object also reaches the detector array via transmission by the second beam splitter. An off-axis hologram [1] can be recorded by adjusting the tilt of the second beam splitter, thus changing the angular separation between the reference and object beams. A digital representation of the complex-valued field, $F_0(x,y)$, from the coherently illuminated object can be obtained from such an off-axis hologram [2] by

1. Fourier transforming the hologram intensity data.
2. Shifting the holographic image of the object to the origin of the Fourier domain.
3. Multiplying by a window function, centered about the holographic image, to eliminate the holographic twin image and the reference and object beam autocorrelation terms.
4. Inverse Fourier transforming to obtain $F_0(x,y)$.

Additionally, artifacts related to edge effects and the use of fast Fourier transforms (FFTs) to perform the Fourier transforms can be suppressed by using another window function both before step 1 and after step 4.

A coherent image of the object, $f(\xi,\eta)$, can be computed by propagating $F_0(x,y)$ to the nominal object plane. In the case of a sufficiently large distance between the object and detector array, $f(\xi,\eta)$ is simply the Fourier transform of $F_0(x,y)$. In practice, the quality of such a computed image can be degraded by phase errors in the object and/or reference beams due to errors in the beam splitters and reference flat or atmospheric turbulence. In the geometry of Fig. 1, the effect of phase errors can be explored by placing an aberrating phase screen between the object and the second beam splitter. A number of algorithms exist for correcting phase errors in the plane of the detector array [3–7]. In such cases, the aberrated far field of the object, $G_0(x,y)$, (obtained from a digital hologram using steps 1–4 listed above) is assumed to have the following form:

$$G_0(x,y) = F_0(x,y)\exp[i\phi(x,y)], \tag{1}$$

where $\phi(x,y)$ is the phase error that is assumed to be close to the plane of the detector array. However, a phase error $\theta(u,v)$, in another plane some distance before the detector array, will introduce anisoplanatism. Figure 2 is a ray diagram, which shows that in such cases ray bundles, originating from different points on the object, pass through different portions of the phase screen on their way to the detector and thus acquire different phase errors. The amount of anisoplanatism in the computed imagery will depend on the distances between the object and the phase screen, z_1, and between the phase screen and the detector array, z_0-z_1, as well as on the widths of the object and the detector array and the details of $\theta(u,v)$. A feature of coherent imaging is that, in such cases, the aberrated object field in the plane of the detector array may be propagated digitally back to the phase screen (distance$=z_0-z_1$) to obtain the aberrated object field, $G_1(u,v)$, in the plane of the phase screen, having the form

$$G_1(u,v) = F_1(u,v)\exp[i\theta(u,v)], \tag{2}$$

where $F_1(u,v)$ is the complex-valued object field that would exist in the (u,v) plane in the absence of the phase error $\theta(u,v)$. Once the field $G_1(u,v)$ is computed, any of the phase-error correction algorithms originally formulated for phase errors of the form of Eq. (1) can be directly applied to $G_1(u,v)$ to correct for the phase error $\theta(u,v)$.

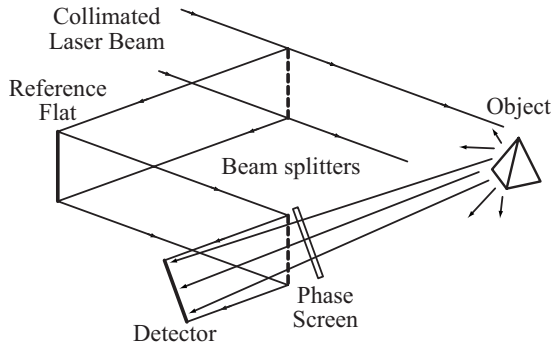

Fig. 1. Setup for recording digital holograms.

Such an approach will yield a computed image with uniform phase error correction across the field of view, i.e., an isoplanatic image. Here, we present experimental results of such an approach to correcting anisoplanatic phase errors in digital holography.

The experimental setup is essentially the same as the diagram shown in Fig. 1. An argon-ion laser, operating in a single longitudinal mode at a wavelength $\lambda=514$ nm and a power of approximately 350 mW, was used as a source. The laser beam was spatially filtered, expanded, and collimated to form a beam approximately 50 mm in diameter. Both beam splitters and the reference flat were 50.4 mm diameter, uncoated, fused silica windows with a 3-deg wedge angle between the front and back surfaces of each window. Using these windows, the object illumination beam received most of the laser power, and the reference beam power was reduced to be only about 2 orders of magnitude larger than the object beam power (after reflection/scattering by the object) at the detector array instead of 3–4 orders of magnitude larger that would occur using 50:50 beam splitters and a mirror for the reference flat. The wedge angles allowed extra reflections from the back surfaces of the windows to walk out of the path of the reference beam before reaching the detector plane. The object was a miniature toy tractor with a width of about 15 mm. The object was used in the system as obtained from the original manufacturer, i.e., the object was not painted or modified to increase its reflectivity. The body of the tractor had been painted with glossy green paint, while the wheels were diffuse yellow plastic. The nominal distance, z_0, between the object and the detector was approximately 1.3 m. The detector array was a complementary metal-oxide semiconductor (CMOS) sensor with 1024×1280 pixels and a pixel pitch of 6.7 μm. Coherent imagery was computed using only a 1024×1024 square area of pixels, giving an effective detector array width of 6.86 mm. The exposure time for a single hologram was 90 ms. Recorded holograms were saved as

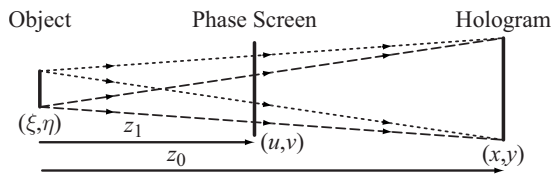

Fig. 2. Diagram showing origin of anisoplanatism when the distance between the phase screen and the detector array is nonnegligible.

16-bit TIFF files, although the detector array was only a 12-bit sensor. The object was mounted on a rotation stage such that holograms could be recorded with different object speckle realizations by making small rotations of the object between exposures, since phase-error-correction algorithms generally perform better with multiple speckle realizations. Having multiple speckle realizations also enables the computation of speckle-reduced images of the object by incoherently averaging speckled image realizations. The phase screen used to introduce aberrations in the object beam was an ordinary compact-disc jewel case and was located approximately $z_0-z_1=100$ mm away from the detector.

First, several holograms were recorded without the phase screen to yield imagery that serves as a baseline for comparison with imagery obtained with the phase screen. A total of $N=10$ holograms were recorded with different object speckle realizations. Each hologram was processed (using the procedure given above) to yield N complex-valued fields from the object, $G_{0,n}(x,y)$ where the subscript $n\in\{1,2,\ldots,N\}$ represents different object speckle realizations. In general, these fields contain a large amount of defocus (associated with the quadratic phase term outside of the Fresnel and Fraunhofer diffraction integrals [6]) and small phase errors associated with imperfect optics. We used a squared-intensity sharpness metric, M, to correct for these errors. If $\hat{\phi}(x,y)$ is an estimate of the phase errors, the associated estimate of the unaberrated fields from the object are

$$\hat{F}_{0,n}(x,y)=G_{0,n}(x,y)\exp[-i\hat{\phi}(x,y)], \tag{3}$$

and the corresponding speckle-averaged image is

$$\hat{I}(\xi,\eta)=\frac{1}{N}\sum_n|\hat{f}_n(\xi,\eta)|^2, \tag{4}$$

where $\hat{f}_n(\xi,\eta)$ is the FFT of $\hat{F}_n(x,y)$, and the value of the sharpness metric M is given by

$$M=\sum_{(\xi,\eta)}\hat{I}^2(\xi,\eta). \tag{5}$$

The use of such sharpness metrics for aberration correction is based on [4–8]. The metric given in Eq. (5) is maximized by finding a phase-error estimate that broadens the histogram of $\hat{I}(\xi,\eta)$, with particular emphasis placed on making bright points in the image brighter [6]. The performance of this metric is expected to be favorable in this experiment, as the imagery contains a number of bright glints. In [8] the issues of regularization and the encountering of local extrema when using sharpness metrics are addressed. We used a polynomial expansion to parameterize $\hat{\phi}(x,y)$, which is a form of regularization that prevents the algorithm from converging to an unrealistic solution containing phase vortices. A conjugate-gradient routine was used to find the polynomial coefficients that maximize M. Figure 3 shows results of using this approach for phase-error correction. Figure 3(a) shows $\hat{I}(\xi,\eta)$ when $\hat{\phi}(x,y)$ is constrained to be a rotationally symmetric quadratic polynomial, i.e., correction of defocus only. While the quality of this image is good, Fig. 3(b)

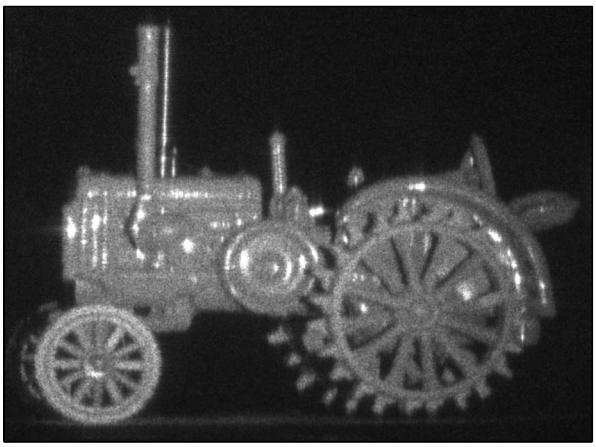

(a)

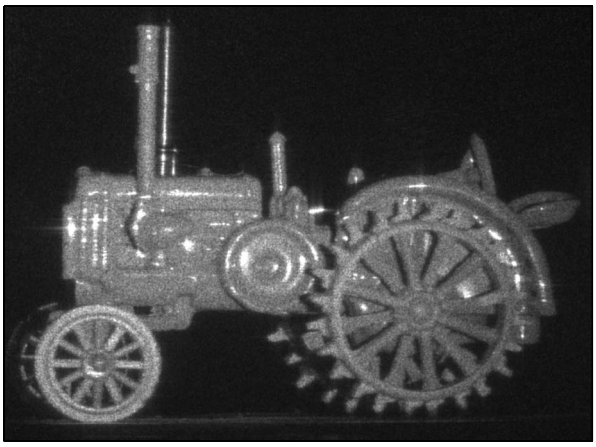

(b)

(c)

Fig. 3. Experimental results obtained without the phase screen: (a) speckle-averaged image correcting for defocus only, (b) speckle-averaged image using a 12th-order polynomial to correct for nominal phase errors in the system, (c) phase-error estimate, moduluo 2π (black=$-\pi$, white=π) used to compute (b).

shows $\hat{I}(\xi,\eta)$ using a 12th-order polynomial expansion (with a total of 91 terms) for $\hat{\phi}(x,y)$ and Fig. 3(c) shows the corresponding $\hat{\phi}(x,y)$ (with piston, tip, tilt, and focus terms subtracted). Note that several of the glints (presumably specular reflections from the paint) on the object appear sharper in Fig. 3(b) than they do in Fig. 3(a). Figure 3(c) indicates that the majority of the phase errors in the nominal experimental setup is ~0.9λ peak to valley of astigmatism due presumably to phase errors in the beam splitters and reference flat. Figure 3(b) serves as a baseline image for comparison with results obtained from holograms recorded with the phase screen. Figure 4 shows magnified portions of Figs. 3(a) and 3(b) to better illustrate the differences between the images.

Another ten holograms were recorded with the phase screen in the object beam path. Again, each hologram was processed as described above to yield the aberrated fields from the object, $G_{0,n}(x,y)$. Figure 5 shows the corresponding results obtained with the phase screen, using the conventional approach of attempting to compensate for an isoplanatic phase error $\phi(x,y)$ near the detector plane. Figure 5(a) shows that with only defocus correction, the phase screen has caused significant blurring of $\hat{I}(\xi,\eta)$ compared to the baseline image. Figure 5(b) shows the results obtained using a 12th-order polynomial phase error estimate $\hat{\phi}(x,y)$, shown in Fig. 5(c). Notice that glints in the region of the tractor engine appear nearly as sharp as they do in the baseline image, while the glints around the rear wheel of the tractor are significantly blurred compared with the baseline. Close comparison with the baseline image also indicates that lower contrast features in the vicinity of the tractor engine are fairly sharp, while the low-contrast features are quite blurred in the regions around the front and rear wheels. The intensity-squared sharpness metric essentially finds a phase error estimate that stretches the histogram: makes the bright points in the image brighter and the dim points dimmer [6]. Since there are several bright glints in the region of the tractor engine, it is not surprising that the sharpness algorithm would converge to a $\hat{\phi}(x,y)$ that corrects for phase errors seen by ray bundles emanating from this region of the object. Due to the finite separation between the phase screen and the detector array, this $\hat{\phi}(x,y)$ does not correct

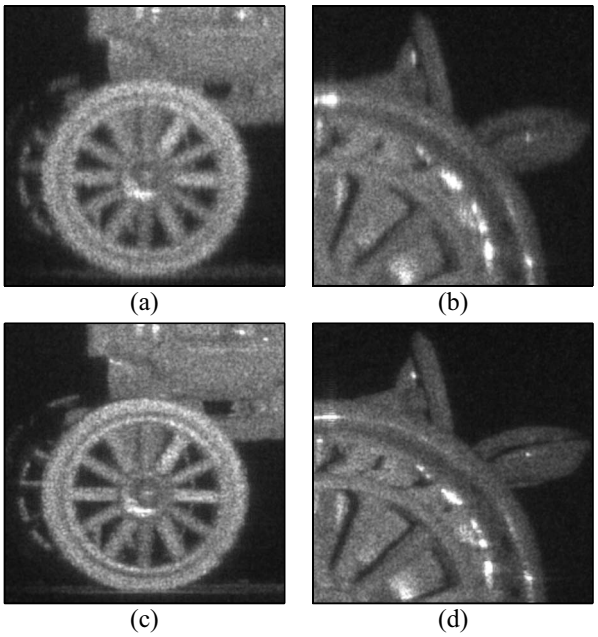

(a) (b) (c) (d)

Fig. 4. (a) and (b) show magnified portions of Fig. 3(a), the speckle-averaged image correcting for defocus only, and (c) and (d) show magnified portions of Fig. 3(b), with a 12th-order polynomial phase-error correction.

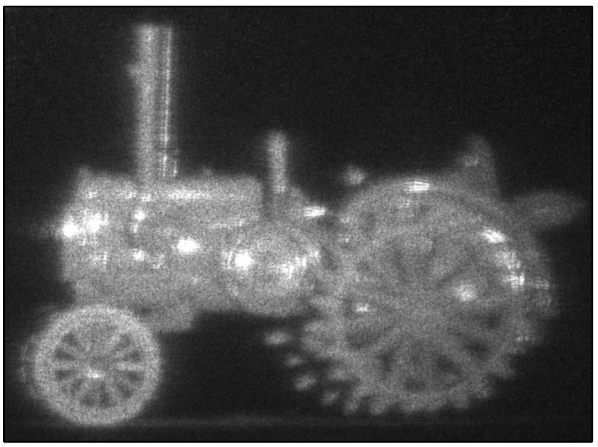

(a)

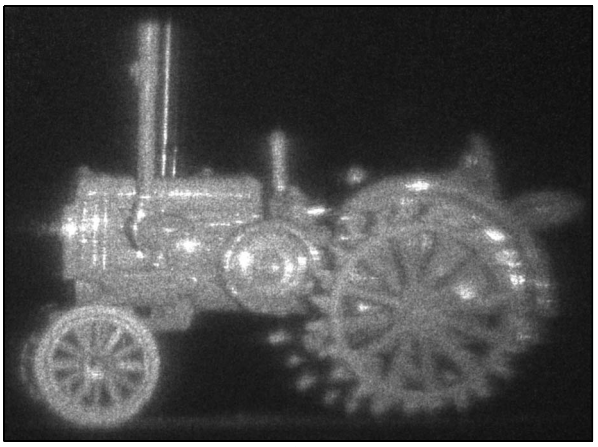

(b)

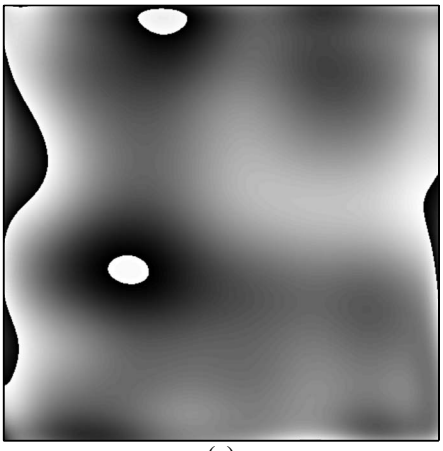

(c)

Fig. 5. Experimental results obtained with the phase screen and attempting to compensate in the plane of the detector array for a phase error that is actually in the plane of the phase screen: (a) speckle-averaged image correcting for defocus only, (b) speckle-averaged image using a 12th-order polynomial to correct for nominal phase errors in the system, (c) phase-error estimate, modulo 2π, used to compute (b). Note the space variance of the residual blur in (b).

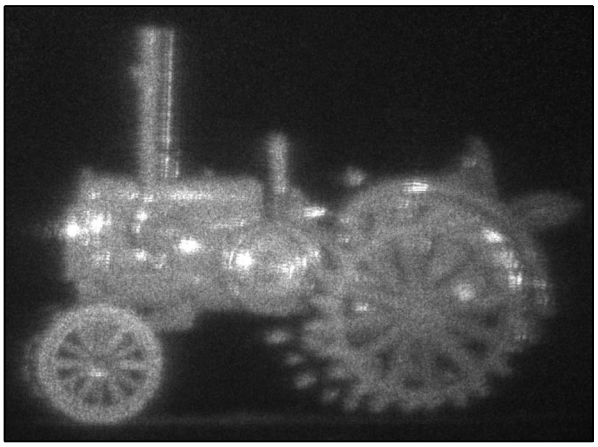

(a)

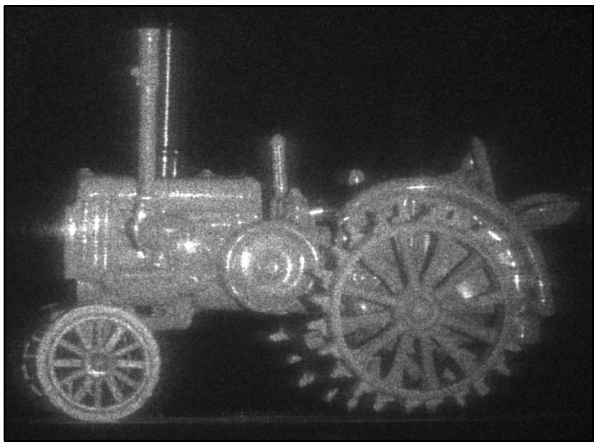

(b)

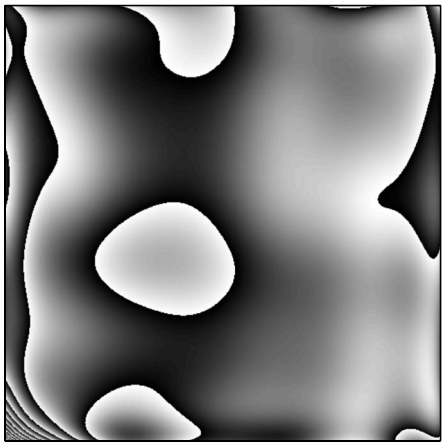

(c)

Fig. 6. Experimental results obtained with the phase screen by propagating the aberrated fields to the phase screen and correcting for a phase error in that plane: (a) speckle-averaged image correcting for defocus only, (b) speckle-averaged image using a 12th-order polynomial to correct for the phase errors in the system, (c) phase-error estimate, modulo 2π, used to compute (b).

well for the phase errors along rays coming from other portions of the object; thus the image in Fig. 5(b) exhibits anisoplanatism.

As mentioned above, such anisoplanatism can be corrected by first propagating the fields $G_{0,n}(x,y)$ to the phase-screen plane and then using the intensity-squared sharpness metric to form an estimate of the phase error $\hat{\theta}(u,v)$ in that plane. We used an angular spectrum propagator to propagate the fields $G_{0,n}(x,y)$ a distance $z_0-z_1=100$ mm, thus obtaining the aberrated object fields $G_{1,n}(u,v)$ in the plane of the phase screen. For a phase-error estimate $\hat{\theta}(u,v)$, the estimated unaberrated fields in the phase screen plane are given by

$$\hat{F}_{1,n}(u,v) = G_{1,n}(u,v)\exp[-i\hat{\theta}(u,v)], \tag{6}$$

and the corresponding speckle-averaged image and value of the sharpness metric, now a function of $\hat{\theta}(u,v)$ instead of $\hat{\phi}(x,y)$, are given by Eqs. (4) and (5), with $\hat{f}_n(\xi,\eta)$ now given by the FFT of $\hat{F}_{1,n}(u,v)$, instead of the FFT of $\hat{F}_{0,n}(x,y)$. Figure 6(a) shows the results of using the sharpness metric to correct defocus only. Again, compared to the baseline image in Fig. 3(b), this image is significantly blurred due to the phase screen. Figure 6(b) shows the image resulting from a 12th-order polynomial phase-error correction $\hat{\theta}(u,v)$, shown in Fig. 6(c). In this image, both glints and low-contrast features in all regions of the image appear nearly as sharp as they do in the baseline image. Thus, the anisoplanic effect of the phase phase screen has been corrected. Looking closely at Fig. 6(b), a horizontally elongated halo is visible around some of the glints, especially the glint on the front edge of the tractor. This may be a result of high-order residual phase errors, as the phase screen contained fine-scale striations that were predominantly oriented along the vertical direction.

These results demonstrate the correction of anisoplanatic phase errors that result for a single phase screen. In the case of phase errors distributed throughout a volume, phase-error correction would require phase estimates in a number of phase screens throughout the aberrating volume and the correction algorithm would be more complicated to implement. Nevertheless, the results shown here are a step in this direction.

ACKNOWLEDGMENTS

This work was supported by Lockheed Martin Corporation. The authors thank Joe Marron for many useful discussions and suggestions.

REFERENCES

1. E. N. Lieth and J. Upatnieks, "Reconstructed wavefronts and communication theory," J. Opt. Soc. Am. **52**, 1123–1130 (1962).
2. J. W. Goodman and R. W. Lawrence, "Digital image formation from electronically detected holograms," Appl. Phys. Lett. **11**, 77–79 (1967).
3. J. N. Cederquist, J. R. Fienup, J. C. Marron, T. J. Schulz, and J. H. Seldin, "Digital shearing laser interferometry for heterodyne array phasing," Proc. SPIE **1416**, 266–277 (1991).
4. R. G. Paxman and J. C. Marron, "Aberration correction of speckled imagery with an image-sharpness criterion," Proc. SPIE **976**, 37–47 (1988).
5. J. R. Fienup, A. M. Kowalczyk, and J. E. Van Buhler, "Phasing sparse arrays of heterodyne receivers," Proc. SPIE **2241**, 127–131 (1994).
6. J. R. Fienup and J. J. Miller, "Aberration correction by maximizing generalized sharpness metrics," J. Opt. Soc. Am. A **20**, 609–620 (2003).
7. S. T. Thurman and J. R. Fienup, "Phase error correction in digital holography," J. Opt. Soc. Am. A **25**, xxx–xxx (2008).
8. R. A. Muller and A. Buffington, "Real-time correction of atmospherically degraded telescope images through image sharpening," J. Opt. Soc. Am. **64**, 1200–1210 (1974).